



## A standard model for the investigation of aerodynamic and aerothermal loads on a re-usable launch vehicle - second stage geometry

Moritz Ertl<sup>1</sup>, Tamas Bykerk<sup>2</sup>

### Abstract

This paper presents a generic geometry for the study of aerodynamic and aerothermal behaviour of an upper stage compatible with the RFZ model, a generic, open source geometry of a re-usable launcher. The vehicle design is presented, outlining simplifications made to retain key features of the vehicle while ensuring a manufacturable and meshable geometry. Computational studies will be performed at altitudes between 70 and 90 km, reflecting the phase directly after staging up to the limits of the continuum flow regime. The geometry and results will be made openly available to the research community to promote collaboration in understanding the design challenges associated with re-usable launchers.

Keywords: *open source geometry, reusable launchers, upper stage, RFZ-Model, CFD*

### 1. Introduction

Aeronautical engineers have a long history of developing standardized models for wind tunnel calibrations and data comparisons between facilities. They are extremely useful in providing baseline datasets for correlation of results, data repeatability over time and verifying model installation or data acquisition systems. Reference models are also particularly relevant from the perspective of numerical analyses, where different codes can be directly compared with each other or assumptions and solver settings can be experimented with to determine solution sensitivity to certain parameters. A standardized reference model typically fulfills two main criteria: Firstly, they are simplistic in shape with a precisely defined geometry and secondly, they are representative of realistic configurations to ensure that the results are relevant. Examples of existing standard models include the AGARD-B [1], ONERA-M [2] and the Standard Dynamics Model (SDM) [3], which have been circulating for decades. Recently, models such as the NASA CRM [4] and the SSAM-Gen5 [5] provide more up to date and relevant aircraft geometries from the past 10 to 20 years.

While aeronautical engineers are well covered with standard aircraft models, the space community is not. Given the sudden and urgent interest in re-usable spacecraft over the past decade, a reference model is lacking, which can serve the research community in facilitating validation of numerical techniques in the generation of aerodynamic and aerothermal data over the entire trajectory. The purpose of this paper is to build on previous work [6] and introduce an upper stage geometry of a re-usable launch vehicle (RLV), where computational models and results will be made openly available to the research community. It is envisioned that this model will serve as a consistent validation case to promote collaboration and further research into the technical challenges associated with RLVs.

This paper will first introduce the geometry and a reference trajectory based on the flight path of Falcon 9. Next, an overview of the numerical setup used for each of the cases will be presented. This will be followed by some preliminary numerical results. A simulation for the internal nozzle flow is discussed and then used to define inflow boundary conditions for the external aerodynamics simulations. Then the chemistry modelling is investigated by comparing a simulation with post combustion to one with frozen chemistry modelling. Finally, a first set of trajectory points with small angle of attack variations are presented and discussed.

<sup>1</sup>DLR - Deutsches Zentrum für Luft- und Raumfahrt, AS-RFZ, Göttingen, moritz.ertl@dlr.de

<sup>2</sup>DLR - Deutsches Zentrum für Luft- und Raumfahrt, AS-RFZ, Göttingen, tamas.bykerk@dlr.de

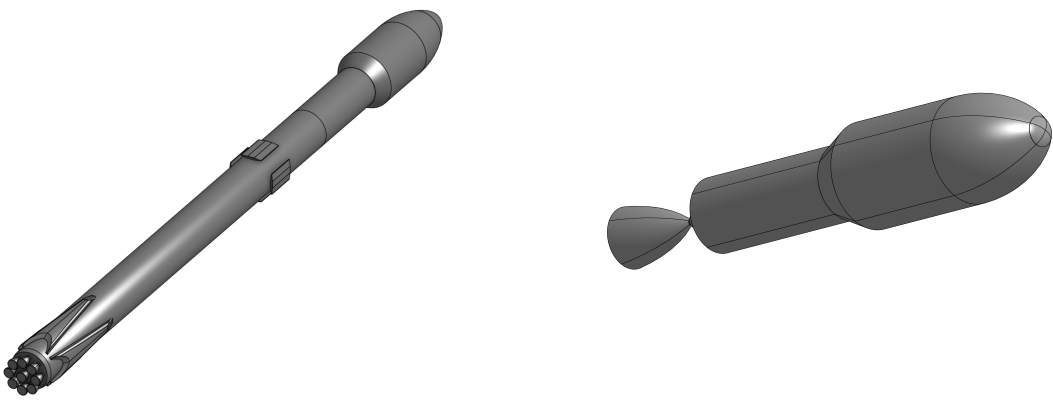
## 2. Methodology

The CFD simulations are done using the well established DLR TAU code [7] with the spacecraft extensions [8]. The TAU code is a second order finite volume solver for sets of conservation equations, in our case the compressible Euler-equations on hybrid structured-unstructured meshes. We simulate with second order spatial accuracy by using the AUSMDV upwinding scheme with a carbuncle fix [9] combined with least squares gradient reconstruction and second order temporal accuracy with a 3-stage explicit Runge-Kutta scheme. For this work we use stationary or quasi-stationary simulations. Combustion is modeled using a finite rate chemistry scheme with the  $CH_4$  reaction mechanism and the reaction rates defined by Zhukov [10].

## 3. Numerical Setup and Geometry

### 3.1. Definition of the Rocket Geometry

The RFZ model is based on the SpaceX Falcon 9 and is presented in Figure 1. This vehicle was chosen because it is the only re-usable launch vehicle which is regularly used for carrying payloads into earth orbit. The geometry was generated using drawings and images of the Falcon 9 freely available on the internet. The vehicle is  $L_{RFZ} = 70\text{ m}$  long with a stage 1 diameter of  $D_{RFZ} = 3.66\text{ m}$ . Some external features of the outer mold line have been omitted in the interest of keeping the vehicle geometry as simple as possible, while still representing the complexity of a RLV. An example of this is the substitution of the grid fins with planar fins. Grid fins require a significant amount of grid points to be represent numerically, resulting in added computational expense. In addition, they would be difficult to manufacture on a small scale, should the model ever be tested in a wind tunnel. Hinge points for the landing legs and externally run lines are also examples of items which have been neglected for simplicity. Various configurations of the first stage exist to be representative of different flight phases.



(a) Launch configuration of the RFZ model

(b) Upper stage of the RFZ model

Fig 1. Isometric views of the open source model geometries

This paper introduces the upper stage geometry as seen in Figure 1b. The stage 2 length is  $L_{ST2} = 28\text{ m}$ . All RFZ variations (launch, landing, aerodynamic glide for these geometries, alongside the other configurations are available for download in ref. [11].

### 3.2. Nozzle Configuration and Operating Conditions

The operating conditions of the nozzle are based on kerosene as a fuel with the combustion chamber pressure set to 108 bar and an oxidiser-to-fuel ratio of 2.35. Initial 1D investigations were made using the NASA CEA tool to determine the species and their respective mass fractions present throughout the nozzle. The mass fractions, pressure and temperature at the combustion chamber exit are used as the boundary conditions for the CFD calculations which are discussed later. The second stage nozzle is based on the vacuum variant of the Merlin 1D+ engine, with an expansion ratio of 165:1 and the same

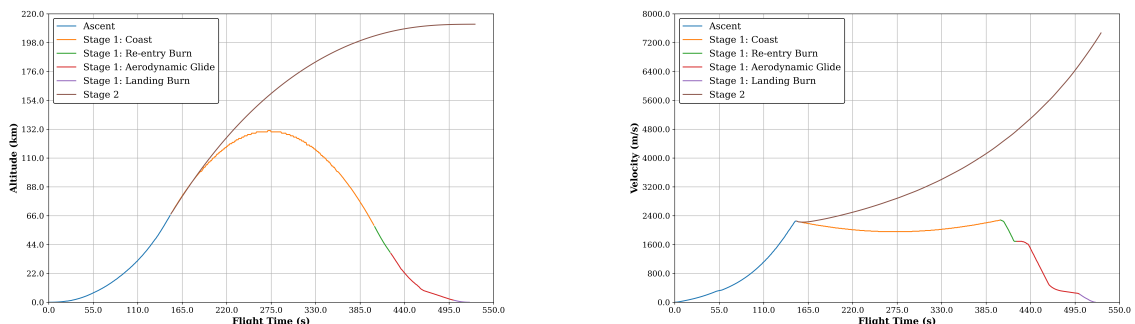
throat radius and length ratio used to define the first stage nozzle geometry. The species at the nozzle exits are summarised in Table 1 where any mass fractions smaller than  $1 \times 10^{-4}$  at the combustion chamber exit have been neglected.

Table 1. Overview of species mass fraction results from NASA CEA analysis for stage 2 engines

Species	Combustion Chamber	Throat	Exit, stage 2
CO	0.44300	0.43407	0.27086
CO <sub>2</sub>	0.24605	0.26014	0.51665
H	0.00114	0.00092	0.00000
H <sub>2</sub>	0.00960	0.00949	0.01980
H <sub>2</sub> O	0.25739	0.264	0.36400
O	0.00366	0.00230	0.00000
OH	0.03058	0.02309	0.00000
O <sub>2</sub>	0.00839	0.00554	0.00000

### 3.3. Trajectory

The stage 2 trajectory is based on the downrange landing scenario, where the first stage booster approximately follows a ballistic trajectory and performs controlled landing on a strategically placed barge downrange from the launch site. For this case, stage separation occurs at approximately 153 seconds into flight at an altitude just below 70 km. The second stage is ejected forwards and the main engine ignites approximately 7 seconds later at an altitude of 76 km and continues to be active until an altitude of 212 km is achieved. For illustration, an overview of the trajectory in terms of altitude and velocity is presented below in Figure 2.



(a) Vehicle trajectory highlighting vehicle altitude at different flight phases

(b) Vehicle trajectory highlighting vehicle velocity at different flight phases

Fig 2. Trajectory representations

### 3.4. Settings and Boundary Conditions

The simulations are set up as laminar, without turbulence modelling, since the highest Reynolds number for all simulations  $Re = \frac{\rho u L_{ST2}}{\mu} = 349\,650 < 5 \times 10^5 = Re_{crit}$  is below the critical Reynolds number. The surfaces of the upper stage are set as viscous walls of laminar subtype with an isothermal wall temperature  $T_w = 300$  K. The far field boundary condition is defined by the velocity  $v$ , the density  $\rho$  and the temperature  $T$  of the inflow. The parameters for the different simulations are provided in table 2.

The initial two simulations are used to study the influence of post combustion chemistry modelling and were done early on based on an now outdated set of parameters given as point 1. The parameters are,

Table 2. Overview simulated trajectory points.

No	Trajectory Point	$h$ [km]	$\rho$ [ $\text{kg m}^{-3}$ ]	$v$ [ $\text{m s}^{-1}$ ]	$T$ [K]	$Ma[-]$	$p$ [Pa]
1	chem mod	-	$9.14 \times 10^{-5}$	2229.72	221.39	7.47	5.82
2	$t = 160\text{ s}$	75.97	$3.45 \times 10^{-5}$	2223.72	206.50	7.72	2.05
3	$t = 165\text{ s}$	80.70	$1.67 \times 10^{-5}$	2232.02	197.20	7.92	0.95

nevertheless, close enough to provide relevant information. The subsequent simulations with parameter variations were done using points 2 and 3, which are points from the RFZ-ST2 upper stage trajectory at select times.

For the purposes of this paper, it is assumed that the upper limit of continuum flow coincides with a flight altitude of 86 km. This is based on the standard atmosphere which assumes that there is perfect mixing of the air and that the molecular weight of the air is the same at all altitudes below 86 km. This permits the use of the hydro-static equation to calculate pressure and density.

A Dirichlet boundary condition is used to model the nozzle outflow boundary. An additional steady state 2D axi-symmetric simulation with a 10,000 points grid is set up. The simulation is run with post-combustion modelling, using the data from NASA CEA combustion chamber calculation as input. The combustion chamber conditions used are  $p_{cc} = 108 \times 10^5 \text{ Pa}$  and  $\rho_{cc} = 8.12 \text{ kg m}^{-3}$  and the species composition provided in table 1 as a pressure reservoir inflow boundary condition. The outflow boundary is set as a pressure outflow with  $p_{exit} = 5.82 \text{ Pa} = p_\infty^{TP1}$  - the ambient pressure for trajectory point 1. The chemistry modelling in the simulation is done using the reaction mechanism by Zhukov [10]. The  $CH_4$  reaction mechanism can be applied for our kerosene fuel rocket, since it provides modelling for all the species present after the combustion chamber. The result of the simulation is shown as Mach number plot with the used computational grid overlayed in figure 3.

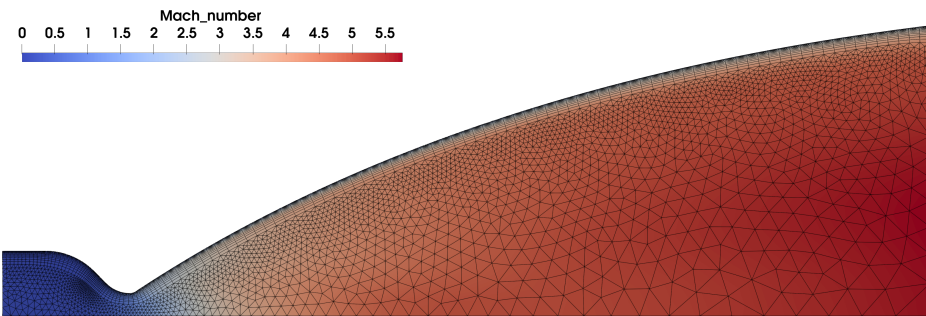


Fig 3. Nozzle simulation result for Mach number with computational grid overlaid.

The results of this nozzle simulation is used to define a Dirichlet boundary condition as the nozzle inflow for the RFZ upper stage simulation. Since the first two rocket simulations are used to investigate the relevance of post combustion on the flow field, there are two ways in which the nozzle simulation results are used. For the simulation with post combustion modelling, the resulting primitive variables and the mass fractions of all the listed species are interpolated onto the nozzle outflow surface of the simulation grid. In this case the fluid for the far field is air represented by the three species  $N_2$ ,  $O_2$  and  $CO_2$ .

The case without post combustion is called the frozen chemistry modelling case. For this case, the species resulting from the nozzle simulation are combined into a single species - called exhaust gas - with the properties of the mixture. The remaining primitive variables are again interpolated onto the nozzle outflow surface of the simulation grid. In this case the fluid for the far field is air represented as second single species with the properties of the mixture of  $N_2$ ,  $O_2$  and  $CO_2$ .

## 4. Results

In this work we present the results for two set of simulations. The first one is an investigation into the chemistry modelling. There, we compare a simulation with full post combustion modelling to one with frozen chemistry. In the second set we establish data for different flight conditions. We provide flow field data and aerodynamic coefficients as first entries for the RFZ-ST2 upper stage in the publicly shared database.

### 4.1. Chemistry Modelling

The simulations on chemistry modelling are done for the parameters of Point 1 from table 2 and with an angle of attack  $AoA = 0^\circ$ . The symmetries of the case were exploited to reduce the computational domain to a quarter model. A coarse grid generated with CENTAUR with 20 prism layers in the boundary and a first layer thickness of  $y^+ < 1.0$  and some initial local refinements in the plume region. Both simulations are run on the coarse grid and then refined several times using the TAU adaptation. The final grid with the adaptations for the frozen chemistry simulation is shown in Fig. 4. The final grid was obtained after five adaptation cycles and consists of over 19 million points.

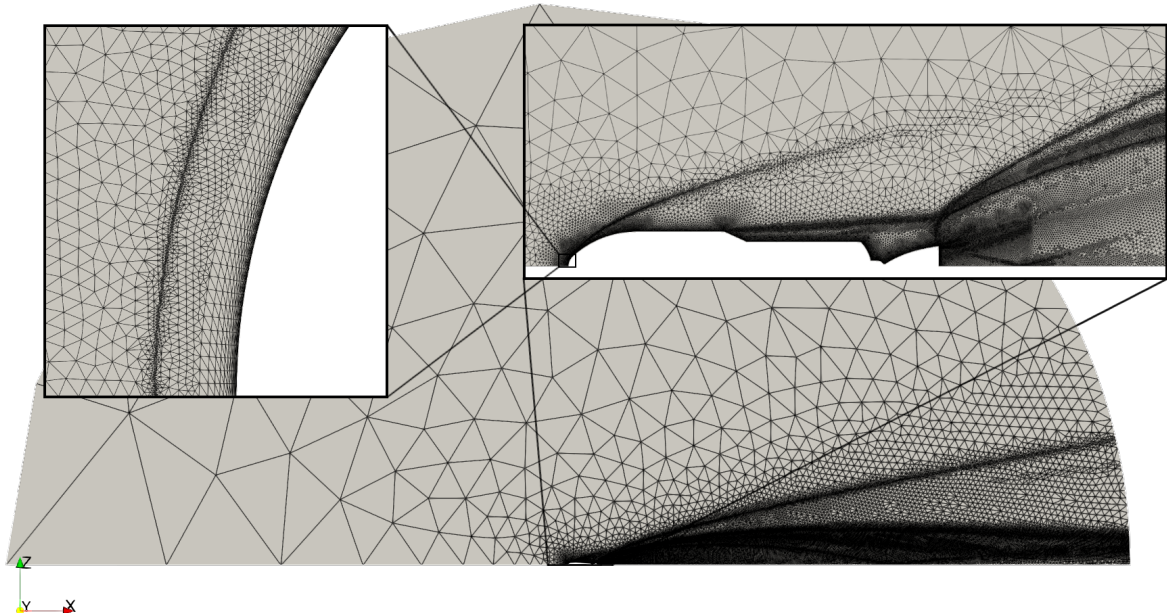


Fig 4. Side view of the quarter mesh with different zoom levels.

Both simulations result in the same flow features, such as positions and angles of shocks and of plume mixing layer. Therefore, to increase the accuracy of the comparison, the simulation with post combustion chemistry is run again on the fine grid of the frozen chemistry simulation. A comparison for both simulations of the Mach number distribution for an overall view of the upper stage and the plume is given in Fig. 5 and provides the general flow field features.

The view is split with the simulations with chemistry modelling being shown in the upper half and the simulation without in the lower half. The axis are made dimensionless with the upper stage length  $L_{ST2}$  to  $x/L$  and  $y/L$ . The nose of the upper stage is situated at  $x/L = 0$  with a shock visible just in front of it. Downstream of the rocket, starting at  $x/L = 1$ , is the plume with a plume core length of  $\approx 10.5L$ . A second shock can be observed just upstream of where the air flow meet the plume. All the general flow features are in good agreement between the two simulations. The plume length and width and the position and angles of shocks compare very well indicating that the post combustion modelling has no major influence on the result. To allow for a more in depth analysis, a closer look at different flow field quantities in the vicinity of the upper stage is given in Fig. 6.

An enlarged view of the Mach number is again shown in 6a. This zoomed plot provides a better view

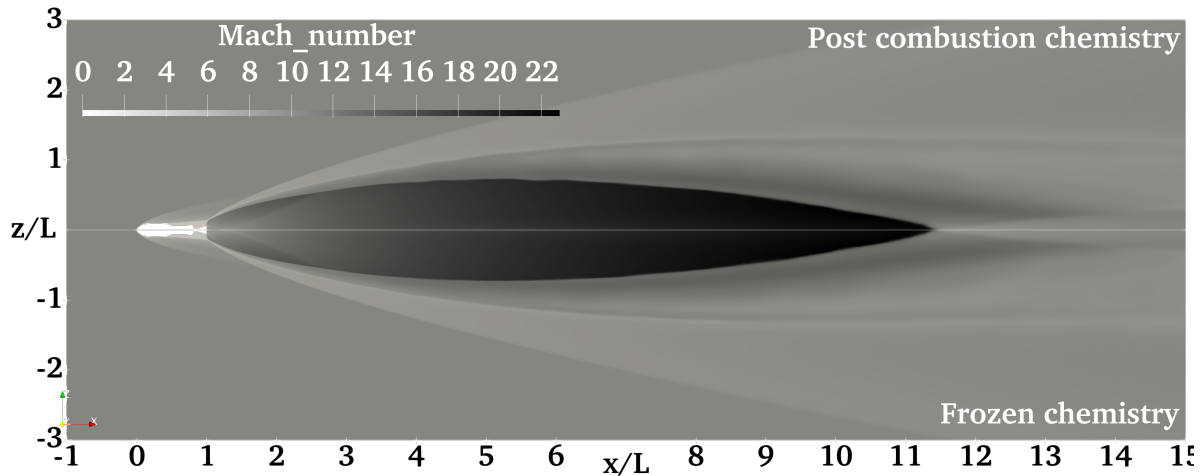


Fig 5. Comparative visualisation of the RFZ-ST2 upper stage chemistry modelling. Mach number for a wide view of rocket, shocks and plume.

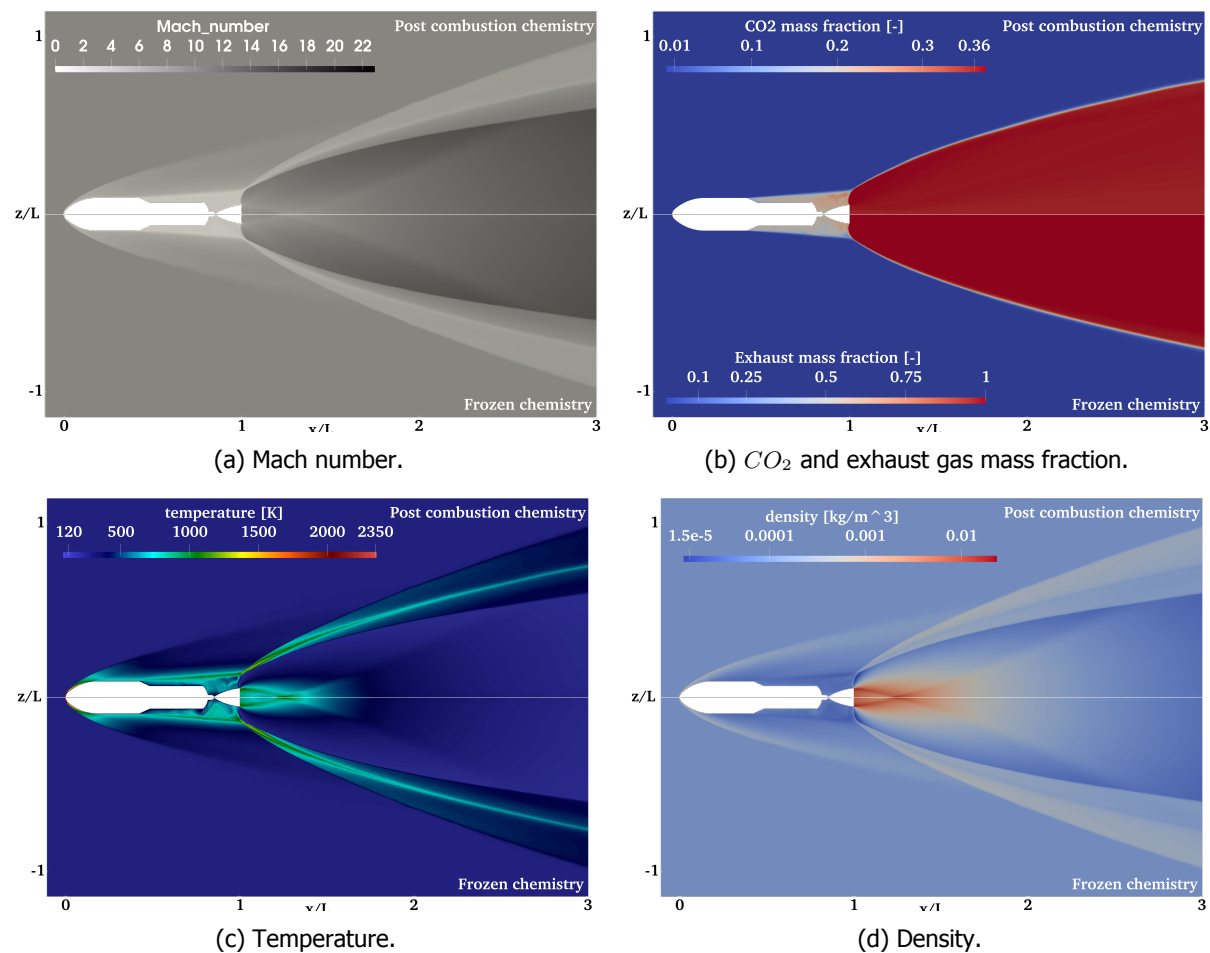


Fig 6. Comparative visualisation of the RFZ-ST2 upper stage chemistry modelling. Zoomed view of the upper stage.

of the flow field around the upper stage and the shock and plume structures. The agreement between the two simulations is still very good. In Fig. 6b the mass fraction distribution for exhaust species are plotted. In the lower half the mass fractions for the "exhaust gas" species is given - the mixture of the species from the nozzle simulation - while in the upper half the mass fractions for  $CO_2$  are shown. The mass fraction of the exhaust species is very evenly distributed throughout the plume and quickly reduces towards the edge of the plume. The distributions are very similar in shape for both simulations. Only the species  $CO_2$ , which composes about 36 % of the exhaust, is shown in this figure for the simulation with chemistry modelling. The shape and distribution for the mass fractions for the other two major product species,  $CO$  and  $H_2O$  with about 36 % and about 25 % respectively, have been analysed and are nearly identical.

In the temperature plot 6c the analysis is similar. The highest temperatures are observed behind the nose shock. Two medium temperature peaks can be seen where the shocks from the nozzle meet at the symmetry plane and at the shock where the plume meets the free flow. There are minor differences in the temperature field in the wake region parallel to the nozzle. This region is highly rarefied, as can be seen in the density distribution 6d. We discuss the limitation of simulating this upper stage at these conditions in our second contribution to this conference [12]. It was very difficult to obtain a fully converged solution in this region and these minor differences and not considered related to the chemistry modelling. For the density distribution the agreement between the two simulations is also very good.

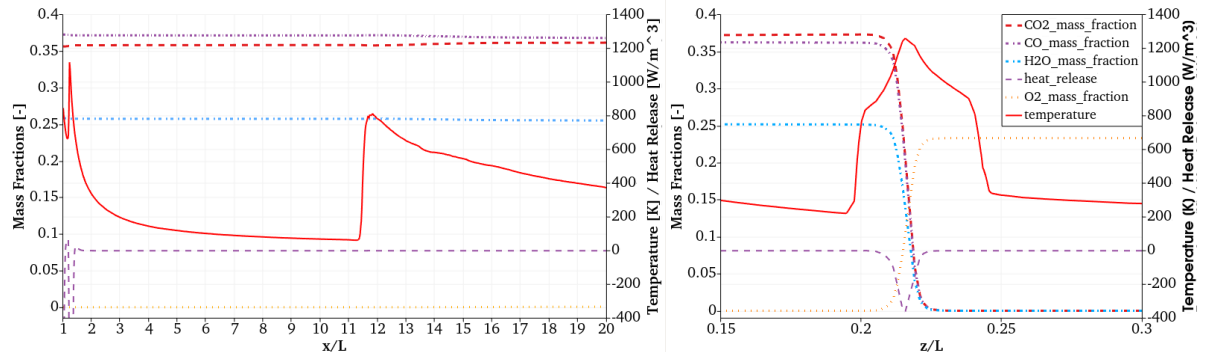


Fig 7. Temperature  $T$ , heat release and mass fractions for  $CO_2$ ,  $CO$ ,  $H_2O$  and  $O_2$  plotted: On the left along the  $x$ -centerline behind the nozzle. On the right along a vertical line at  $x/L = 1.15$  through the plume shear layer from  $z/L = 0.15$  to  $z/L = 0.3$ .

The mass fractions for the product species  $CO_2$ ,  $CO$  and  $H_2O$  as well as for  $O_2$  and  $O$  are plotted, together with the temperature  $T$  and the heat release from chemical reactions in Fig. 7. In the first graph the values are plotted over the  $x$  axis central line at  $y = z = 0$  starting from the nozzle exit. We observe basically no changes in any of the mass fractions, except for minor movement after the nozzle in the region of the oblique shock reflection. A similar behaviour is observed for the temperature, which, after a peak of  $T \approx 1100$  K at the oblique shock reduces to below 200 K in the plume core. The Temperature along the centerline rises to about 800 K at the end of the plume core, but reduces again to below 400 K downstream.

In the second graph the values are plotted along a vertical line through the plume shear layer. The line is situated behind the nozzle exit at position  $x/L = 1.15$  and ranges from  $z/L = 0.15$  to  $z/L = 0.3$ , with values  $z/L < 0.22$  being situated inside the plume. The plot reveals minimal mixing of species, with the mass fractions of the products  $CO_2$ ,  $CO$  and  $H_2O$  being nearly constant inside the plume and then rapidly reducing to zero over the small area of the shear layer.  $O_2$  behaves similarly, with the concentration being constant outside the plume and dropping to zero inside it. For the temperatures, the plot shows small values  $T < 400$  K both inside and outside the plume with the exception of the region around the shock at  $z/L \approx 0.22$ , where values of  $T \approx 1250$  K are reached. The conditions for post combustion would only be given around the shock, given the values of temperature and species

concentrations, however, the heat release at this position is at negative values, indicating endothermic reactions driven by the temperatures from the shock.

Our observations showed that there are no major differences between the two simulations in both the wider flow field and the flow field around the upper stage for a multitude of variables, such as Mach number, density or temperature. It further showed that the mass fractions for the major products in the simulation with chemistry modelling exhibit no visible change in composition and distribution throughout the plume. The shear layer of the plume is identified as the possible location for post combustion. However, the heat release at this location indicates a prevalence of endothermic reactions due to the shock. These observations strongly indicate that post combustion modelling is not relevant at our flight conditions.

#### 4.2. Flight Conditions

We simulate the RFZ-ST2 upper stage for different flight conditions. Two points from the trajectory at times  $t = 160\text{ s}$  and  $t = 165\text{ s}$  are chosen. The points, labeled point 2 and point 3, are provided in table 2. The points will each be simulated under three angles of attack:  $0.0^\circ$ ,  $2.5^\circ$ ,  $5.0^\circ$ . In order to be able to do angle of attack investigations a half model is simulated. The coarse grid was generated with the same settings as for the previous investigation, with 20 prism layers in the boundary and a first layer thickness of  $y^+ < 1.0$  and some initial local refinements in the plume region. A lower resolution is chosen for this production style simulations. The coarse grid is adapted two times for each flight condition resulting in a final grid of over 10 million points. An overview of the simulation results is given in Fig. 8 displaying the Mach number distribution for the six flight conditions.

The figures are arranged to show the increasing angle of attack from top to bottom and the increase in flight altitude from left to right. The two major influences can be easily identified. An increase in angle of attack leads to a deflection of the plume from the symmetry axis. The increase in flight altitude leads to a decrease in air density and, therefore, to a larger plume both in axial and radial extension.

The aerodynamic coefficients for lift  $c_l$  and drag  $c_d$  for all investigated flight conditions are given in table 3. The coefficients are calculated using a reference area

$$A_{\text{ref}} = \frac{1}{2}\pi \left( \frac{D_{\text{RFZ}}}{2} \right)^2 = 5.260 \text{ m}^2, \quad (1)$$

where the diameter of the first stage diameter  $D_{\text{RFZ}}$  is chosen for consistency of the database and the factor  $\frac{1}{2}$  is due to the simulated geometry being a half model. The changes in aerodynamic coefficients for different flight conditions are consistent with theory. An increasing angle of attack leads to an increase in both lift and drag.

Table 3. Overview of aerodynamic coefficients for select trajectory points.

Trajectory Point	Angle of Attack	Lift coeff. $c_l$	Drag coeff. $c_d$
2 $t = 160\text{ s}$	$0.0^\circ$	-0.0017	0.9949
2 $t = 160\text{ s}$	$2.5^\circ$	0.1099	1.0081
2 $t = 160\text{ s}$	$5.0^\circ$	0.1761	1.0239
3 $t = 165\text{ s}$	$0.0^\circ$	0.0062	1.0490
3 $t = 165\text{ s}$	$2.5^\circ$	0.0715	1.0636
3 $t = 165\text{ s}$	$5.0^\circ$	0.1418	1.0909

A more detailed look into the flow fields for temperature and density and into the surface heat flux for select flight conditions is provided in Fig. 9. The differences from altitude are the comparison between the middle row for point 2 and the lower row for point 3. The flow field around the upper stage as well as the forward part of the plume are very similar. The greater radial expansion of the plume becomes noticeable downstream. The differences from angle of attack for point 2 are the comparisons between the upper row with  $\text{AoA} = 5.0^\circ$  and  $\text{AoA} = 0.0^\circ$ . Here the influence of the velocity component in  $z$  can

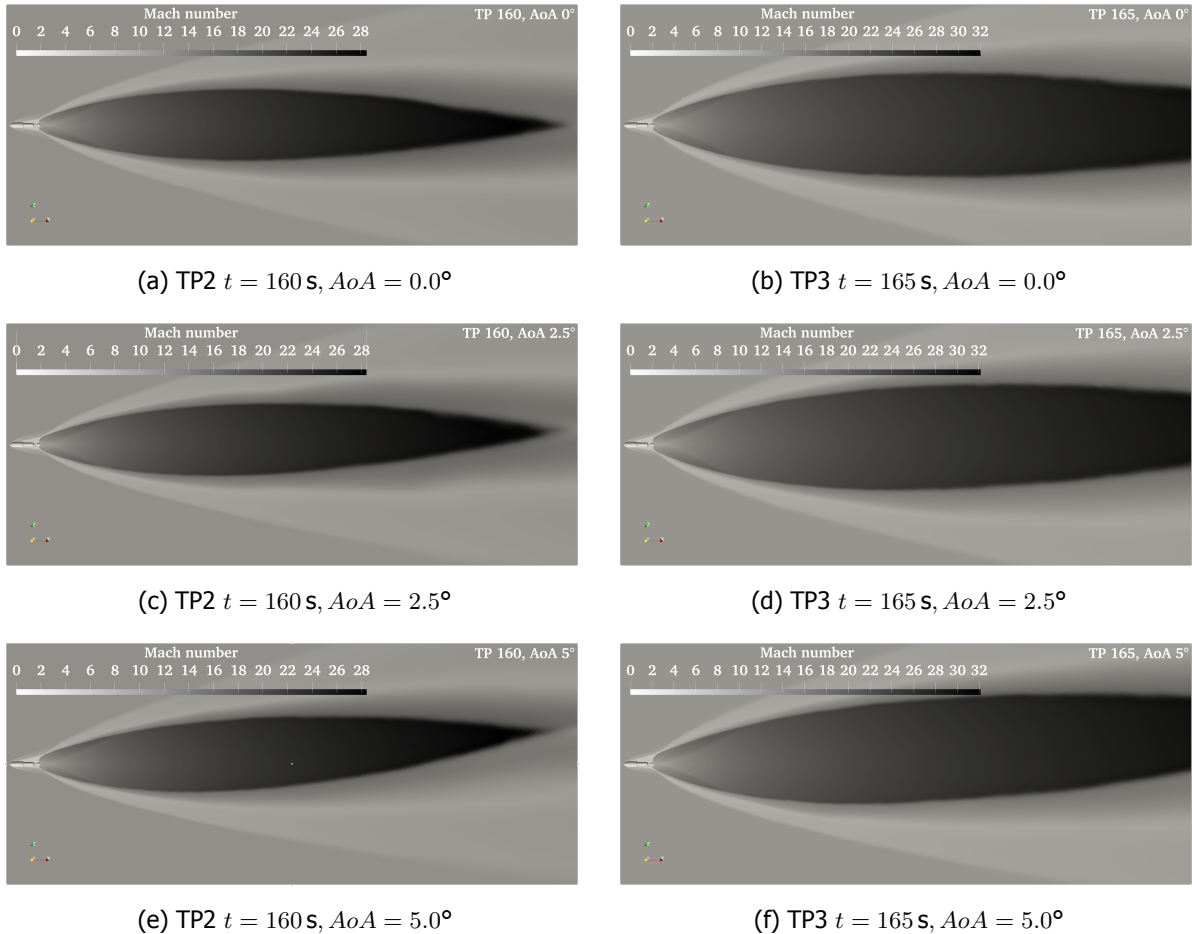


Fig 8. Mach number fields for the simulated trajectory points

be clearly seen. For the  $5.0^\circ$  case in Fig. 9c the region with higher temperatures is compressed closer to the vehicle on the windward side, while it expands on the lee side. The influence of the angle of attack can also be observed in the shape of the plume.

The surface heat fluxes can be seen on the left column. In order to provide a good visualisation the result was rotated around its axis, so that in these case the angle of attack is moving clockwise. Comparing 9d with 9f we can see that the heat flux reduces slightly for the higher flight condition, due to the decrease in density. Fig. 9b shows, that the angle of attack skews the surface heat flux distribution on the upper stage, increasing the heat fluxes to the windward side. A cross check for the heat flux results was performed by calculating an estimate for the stagnation point heat flux with the Sutton-Graves law [13]. The estimate is  $q_{SG} = 1.1 \times 10^4 \text{ W m}^{-2}$ , strongly supporting the validity of the simulation results.

## 5. Conclusion and Outlook

The purpose of this work is the introduction of the open source RFZ model for the upper stage for a re-usable launcher to the scientific community. The RFZ model aims to be a standardised model that helps to facilitate open scientific exchange on re-usable launchers and provides geometry data, trajectory data and boundary conditions. This data, as well as research results from this paper, are shared on [14]. We support the publication of the geometric data and the boundary conditions by additionally providing a first set of CFD simulation results done with the DLR Tau code. We describe our simulation process, including the numerical settings, the geometry and the definition of the nozzle boundary condition. We

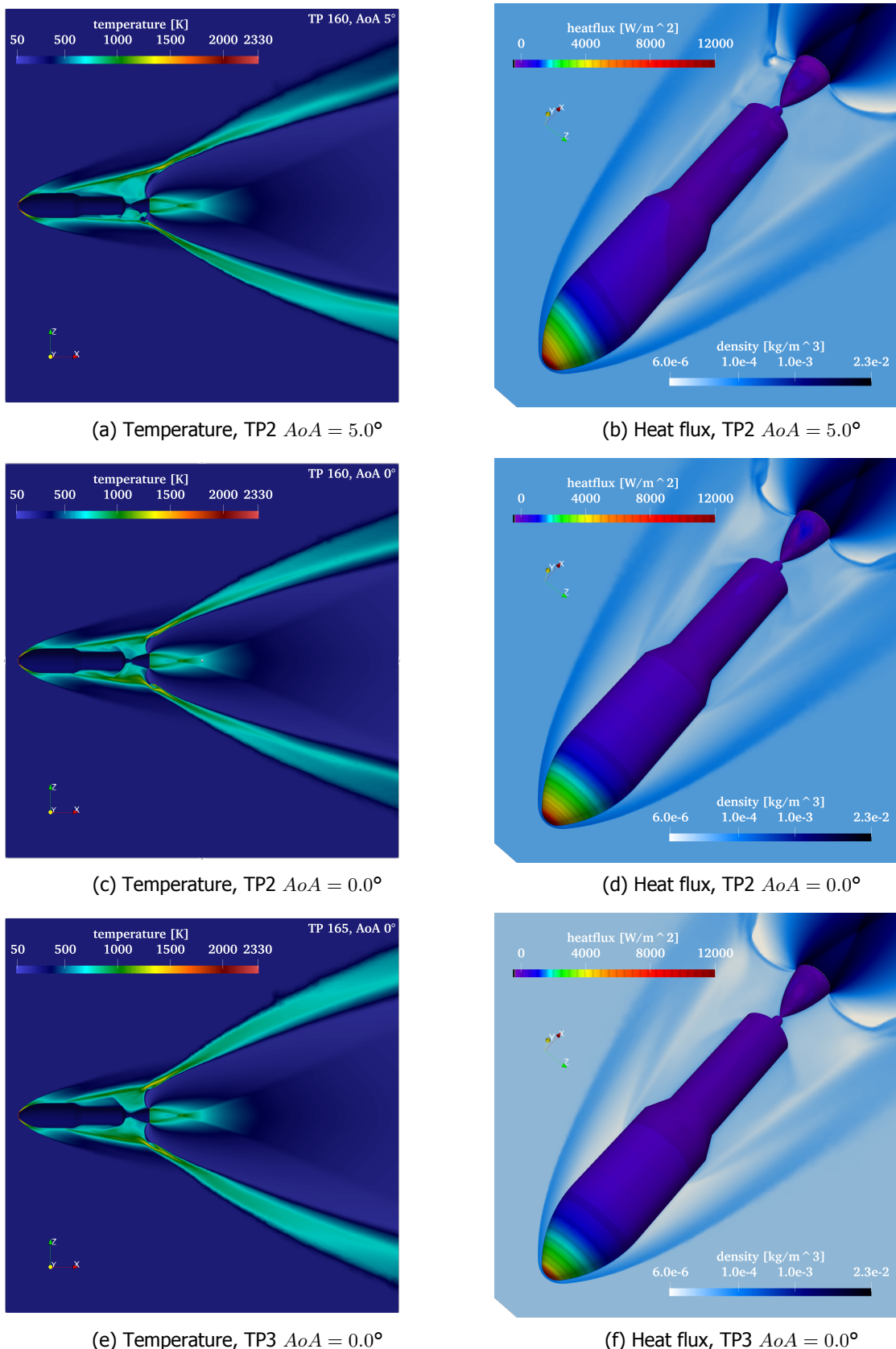


Fig 9. Visualisation of temperature and surface heat flux and density.

analyse the influence of the chemistry modelling, showing that for the investigated trajectory points a post combustion modelling is not necessary. We investigate different flight conditions and provide result data on the flow field, aerodynamic coefficients and surface heat fluxes.

## References

- [1] North Atlantic Treaty Organization. Advisory Group for Aeronautical Research and Development. Wind tunnel calibration models - agard specification 2. Technical report, NATO, 1958.
- [2] R.D. Galway and M. Mokry. Wind tunnel tests of onera aircraft models. Technical report, National Aeronautical Establishment, 1977.
- [3] M. Beyers and X. Huang. Subsonic Aerodynamic Coefficients of the SDM at Angles of Attack up to 90°. Technical report, NRC, Ottawa, Canada, 1990.
- [4] M. B. Rivers, J. Quest, and R. Rudnik. Comparison of the nasa common research model european transonic wind tunnel test data to nasa test data (invited). In *AIAA SciTech Forum*, Kissimmee, Florida, Jan 2015.
- [5] Nicholas F. Giannelis, Tamas Bykerk, and Gareth A. Vio. A generic model for benchmark aerodynamic analysis of fifth-generation high-performance aircraft. *Aerospace*, 10(9), 2023.
- [6] Tamas Bykerk. A standard model for the investigation of aerodynamic and aerothermal loads on a re-usable launch vehicle. In *Aerospace Europe Conference 2023 - 10th EUCASS - 9th CEAS, Lausanne, Switzerland*, 2023.
- [7] D. Schwamborn, T. Gerhold, and R. Heinrich. The dlr tau-code: recent applications in research and industry. In *ECCOMAS CFD 2006 CONFERENCE*, 2006.
- [8] Klaus Hanemann, Jan M. Schramm, Alexander Wagner, Sebastian Karl, and Volker Hanemann. A closely coupled experimental and numerical approach for hypersonic and high enthalpy flow investigations utilising the heg shock tunnel and the dlr tau code. Technical report, DLR, 2010.
- [9] Yasuhiro Wada and Meng-Sing Liou. A flux splitting scheme with high-resolution and robustness for discontinuities. In *32nd Aerospace Sciences Meeting and Exhibit*, 1994.
- [10] Victor / V. P. Zhukov and Alan Kong. Skeletal kinetic mechanism of methane oxidation for high pressures and temperatures. In *7th European Conference for Aeronautics and Space Sciences (EUCASS)*, July 2017.
- [11] T. Bykerk. Rfz data repository, 2023. <https://zenodo.org/communities/rfz-model/?page=1&size=20>.
- [12] Leo Basov, Moritz Ertl, and Tamas Bykerk. Comparison of focker-planck and cfd simulations of the rfz-st2 upper stage. In *HiSST: 3rd International Conference on High-Speed Vehicle Science & Technology, 14–19 April 2024, Busan, Korea*, 2024.
- [13] K. Sutton and R.A. Graves. A general stagnation point convective heating equation for arbitrary gas mixtures. Technical report, NASA, 1971.
- [14] Tamas Bykerk. The rfz model - a standard model for the investigation of aerodynamic and aerothermal loads on a re-usable launch vehicle. <https://zenodo.org/communities/rfz-model>. Accessed: 2023-09-16.